High-throughput bend-strengths of ultra-small polysilicon MEMS components

Robert F. Cook,[1] Brad L. Boyce,[2] Lawrence H. Friedman,[3] Frank W. DelRio,[2,*]

[1]Winterville, NC 28590, USA

[2]Material, Physical, and Chemical Sciences Center, Sandia National Laboratories, Albuquerque, NM 87185, USA

[3]Material Measurement Laboratory, National Institute of Standards and Technology, Gaithersburg, MD 20899, USA

[*]Address correspondence to: Frank W. DelRio, fwdelri@sandia.gov

Abstract

The strength distribution of polysilicon bend specimens, approximately 10 μm in size, is measured using a high-throughput MEMS fabrication and testing method. The distribution is predicted from reference tests on tensile specimens and finite element analysis of the bend specimen geometry incorporated into a stochastic extreme-value strength framework. Agreement between experiment and prediction suggest that the ultra-small specimens may be at the limit of extreme-value scaling and contain only one strength-controlling flaw/specimen.

A critical element in mechanical design is the prediction of the load-bearing capacity of structural components from strength information derived from test coupons. For commercial reasons such coupons are usually smaller, less complicated in shape, and fewer in number than the intended components, so that extrapolation is inevitable.[1] For microelectromechanical systems (MEMS), the extrapolation and inherent information leverage are very large, as billions of small-scale components are manufactured and sold commercially[2] and yet only thousands of test coupons are examined mechanically. There is thus an ongoing need for the development and verification of procedures that predict the load carrying capability of MEMS components from limited coupon or test specimen strength data. Recent work in this area has advanced on two fronts. First, a range of experimental configurations have been developed that enable the strengths of large numbers of MEMS test specimens to be measured reasonably quickly.[3-5] Most prominent amongst these, and the test vehicle that will be used here, is the slack chain configuration[3] that permits 1000 silicon (Si) MEMS specimens to be tested in approximately 16 h. Such numbers greatly improve the precision of design predictions. Second, an analytic framework based on stochastic extreme-value theory has been developed that enables quantitative strength comparisons between specimens of different sizes and shapes. The framework also enables interpretation of strengths in terms of an underlying invariant material flaw population and greatly improves the accuracy of design predictions.[4] The framework has been applied in interpretation of strength data in terms of flaw size distribution and spatial density from MEMS tensile specimens with straight sides, notches, and corner fillets.[6-8] The emphasis on flaws derives from the brittle behavior of Si at room temperature—component and test specimen failure are determined by fracture from strength-controlling flaws. Comprehensive reviews of strength and other mechanical behavior of Si are given elsewhere.[9,10]

In this Letter, a further application of the high-throughput experimental method combined with the physics-based analytical framework is used. The application extends the earlier work[6-8] in three major ways: (i) First, a specially-designed specimen will enable strength in *bending* to be measured. (ii) Second, the bending strength distribution will be *predicted* from tensile strength measurements. (iii) Third, the bending specimen is extremely *small*, possibly the smallest tested (4.78 μm long, as opposed to previous reports that utilized clamped-clamped specimens that were 12 μm long[11,12]). This last point has the consequences that prediction here is in the direction of decreased size, as opposed to the earlier increasing-size comparisons,[7,8] and that the specimen may

approach the limit of containing a single flaw and the limit of extreme-value effects, as suggested for small particles.[13,14] Many features of the earlier work are retained: all MEMS specimens are fabricated in polycrystalline silicon (polysilicon) on the same single-crystal Si (SCS) substrate wafer such that the strength controlling flaw population is invariant; finite element analysis (FEA) is used to link specimen failure load and stress state; and, direct microscopic observation is used to assess the validity of the flaw population inferred from strength measurements. The overarching objective of this work is the further development and verification of procedures that predict the load carrying capability of MEMS components from limited coupon or test specimen strength data and enable quantitative strength comparisons between specimens of different sizes and shapes.

Many MEMS configurations have been developed to load small-scale test specimens in bending, including beams of SCS[15-22] and polysilicon[23-27] formed by MEMS processes and SCS beams formed using a focused ion beam.[28-34] The polysilicon beams examined here were fabricated using the SUMMiT V MEMS process (reticle set RS784). Multiple slack chains, each containing 12 interconnected beams, were fabricated from poly3 material in a configuration similar to those examined earlier.[3,7,8] The configuration enables independent, sequential determination of the failure load, F_f, for each beam. A set of the first five beams in a chain and the associated loading ring are shown in Fig. 1(a). A single beam is illustrated in Fig. 1(c). Comparison with Fig. 1(a) shows that loading of a chain via the ring leads to bending of the beam via end displacement in a clamped-clamped geometry, similar to that in recent studies.[21,22] Scanning electron microscope (SEM) measurements of beam dimensions showed that the central, uniform cross-section of the beam was 4.78 μm long × 1.34 μm wide with larger sections either side formed by circular end tabs with approximately 6.7 μm radii. The poly3 layer of the SUMMiT V process generated beam thicknesses of 2.33 μm with plan dimensional dispersion of 0.04 μm.[7,8] As part of the same process, chains of uniform section tensile bars, 21.72 μm long × 1.95 μm wide, similar to those studied earlier[7] were also fabricated, as shown in Fig. 1(b) and Fig. 1(d).

Chains of bend and tensile specimens were tested as described earlier,[3,7,8] generating 97 bend bar failures in the load domain 0.5 mN to 1 mN and 127 tensile beam failures in the load domain 10 mN to 13 mN. The failure stress, or strength σ_f, for each tensile bar was evaluated from the failure load by $\sigma_f = F_f/bd$, where b and d are the thickness and width of the bar, respectively, and bd is recognized as the cross-sectional area (the linear load-stress relationship is appropriate herein, given that non-linear material and/or geometric effects are negligible[3,7,8]). A lower bound estimate

for the failure stress of the bending beam is obtained by recognizing that the clamped-clamped configuration consists of two joined cantilevers, half the length of the beam each. The maximum outer fiber stress in each cantilever is given by $\sigma_f = Mc_n/I$, where $M = F_f L/2$ is the moment exerted on each cantilever and L is the beam length, $c_n = d/2$ is the distance from the outer fiber to the beam neutral axis, and $I = bd^3/12$ is the second moment of area of each cantilever. Combining these terms gives an expression for the strength of the beam, $\sigma_f = K_b F_f/bd$, where $K_b = 3(L/d)$ is a stress concentration factor. The dimensions given above gives $K_b \approx 10.7$, such that the observed failure loads above for the tensile and bending specimens represent similar strengths. In particular, a load of $F_f = 1$ mN applied to the structure in Fig. 1 (c) results in an estimated peak tensile stress in the beam of $\sigma = 3.43$ GPa. This stress is a lower bound as the end tabs increase the cantilever moment arm, although the effect is countered by an increase in width of the bent tab section. Hence, peak tensile stresses are expected to occur in the outer fibers of the narrow central section of the beam but the numerical values are expected to be slightly greater than the above estimate.

A more thorough assessment of the stress state in the loaded beam was performed by implementing a FEA procedure similar to that used earlier,[8] taking into account the macroscopic curved beam+tab shape and microscopic surface roughness evident in Fig. 1. Briefly, the detailed outline of the specimen was extracted from digitized images similar to Fig. 1(c) and input to a commercial FEA program (Comsol, Burlington, MA). The elastic stiffness matrix of the specimen was calculated assuming [111] pencil-like texture for the polycrystalline array of grains, resulting in Reuss-averaged in-plane extension moduli[10] of $E = 169.2$ GPa and $\nu = 0.262$. FEA simulations of the stresses generated in the specimen were performed at two spatial resolutions (44.7 nm and 223.3 nm) with 1 mN longitudinal loading of the specimen implemented using rigid-displacement boundary conditions and plane-stress constraint. Figure 2(a) shows a color-filled intensity map of the first principal stress σ in the loaded specimen from the highest-resolution simulation. The deformed shape is shown as the bold outline, the undeformed shape is shown as the fine outline. It is clear that loading generates transverse displacements of the end tabs that are accommodated by bending in the central beam. The bending leads to tensile stress in the beam, predominantly in the outer fibers adjacent to the built-in curved sections. Figure 2(b) shows the first principal stress evaluated from both resolution simulations along both the top and bottom outer fibers. Several features are significant: First, the tensile stress is distributed over approximately 8 μm, passing through maxima where the sections increase at the built-in curved ends, about 2.5 μm from the

beam center. Second, there are substantial local variations of the tensile stress about the overall distributions, reflecting the surface roughness, resulting in local peak stresses of approximately 4.5 GPa. Third, the values are in agreement with the simple cantilever lower-bound estimate, shown in Fig. 2(b) as the dashed horizontal line and slightly underestimating the maxima in the overall trends. Fourth, the results from all simulations were similar, suggesting no resolution or location dependence in stress assessment. Overall, two conclusions from the simulations are: (i) the curved shape of the specimen generates an effectively longer and wider beam that results in outer fiber stresses comparable to those estimated for a uniform beam and (ii) surface roughness significantly perturbs the local stress from the ideal variation. The conversion factor for strength/failure load in the bend specimen will be taken here as 4.5 GPa/mN, consistent with Fig. 2(b).

Empirical distribution functions, (edf)s of strength, $Pr(\sigma_f)$, for the tensile bar and bend beam samples[7,8] are shown in Figure 3. The symbols to the left at smaller strengths represent the strengths of the tensile bars; the values are comparable to those measured previously on similarly fabricated and sized bars and the uncertainty is approximately the symbol size (≈1 % to 2 %).[7] The symbols to the right at greater strengths represent the strengths of the bend beams; the bars represent relative uncertainty of ±5 % consistent with the maxima in Fig. 2. The bending strengths are comparable to those measured earlier for MEMS fabricated polysilicon but less than those observed for FIB-fabricated SCS. The solid line to the left is a best fit to the tensile data constrained by prior measurements of flaw density in the poly3 material.[7] The solid lines to the right are predictions of the bend data based on the stochastic extreme-value flaw and strength analysis developed earlier.[6-8] A brief description of the analysis, fit, and predictions follows.

The strength-controlling flaws in polysilicon MEMS occur on specimen sidewalls and are related to grain-boundary grooves formed during fabrication.[3,7,25,35] The flaws are described by an average spatial density expressed as a number/length λ; the mean flaw separation along a sidewall is $1/\lambda$. The size distribution of the flaws is given by a probability density function (pdf) $f(c)$, where c is a crack length. The domain of the pdf is bounded by a minimum and maximum, c_{min} and c_{max}, respectively. The pdf is expressed as the derivative of the cumulative distribution function (cdf) of the flaws, $F(c)$, $f(c) = dF(c)/dc$ and $F(c_{min}) = 0$ and $F(c_{max}) = 1$. The population of flaws in a wafer is an invariant, intensive property, described by λ and $F(c)$. The strength σ_f associated with a flaw is described here by the Griffith equation, $\sigma_f = Bc^{-1/2}$, where B characterizes the toughness of the material and the geometry and stress state of the flaw[36] and has dimensions of MPa m$^{1/2}$. Using the

$\sigma_f(c)$ expression, the conjugate strength cdf describing the population of strengths is given by $F(\sigma_f) = 1 - F(c)$. The strength parameters B and $F(\sigma_f)$ are also invariant and intensive.

A specimen of size $L = k/\lambda$ formed from the population contains k flaws. If the k flaws are probabilistically independent, stochastic extreme-value analysis gives the probability that the specimen will exhibit a strength less than σ_f as[6-8]

$$H(\sigma_f) = 1 - [1 - F(\sigma_f)]^k. \quad (1)$$

Flaw independence is equivalent to the physical assumption of "weakest link" behavior. It is noted that as $H(\sigma_f)$ depends on k, $H(\sigma_f)$ is extensive, and that the relationship between $H(\sigma_f)$ and $F(\sigma_f)$ is independent of the form of $F(\sigma_f)$. If a sample of N specimens, each of size L, is formed from the material described by the population, the edf of the sample $Pr(\sigma_f) \rightarrow H(\sigma_f)$ for $N >> 1$ and $Pr(\sigma_f)$ is a discrete estimator of $H(\sigma_f)$. Data interpretation is made easier through the use of a continuous sample estimator $\hat{H}(\mu)$ formed by functional best fit to $Pr(\sigma_f)$. Here, the parameterized continuous population function[6-8]

$$\hat{F}(\mu) = 30(\mu^{3p}/3 - \mu^{4p}/2 + \mu^{5p}/5) \quad (2)$$

and

$$\mu = (\sigma_f - \sigma_L)/(\sigma_U - \sigma_L) \quad (3)$$

were used to estimate $H(\sigma_f)$ using $\hat{H}(\mu) = 1 - [1 - \hat{F}(\mu)]^k$. The parameters σ_U and σ_L are empirical upper and lower strength bounds of the fitting function, respectively, and $0 \leq \mu \leq 1$ is a relative strength parameter. The function $\hat{F}(\mu)$ results from a perturbed Beta function, where the fitting parameter p determines shape and symmetry. The function $0 \leq \hat{F}(\mu) \leq 1$ is also bounded with 0 derivative at both bounds—the separation of shape and functional behavior at the bounds enables better fits to experimental data. (It is noted that the shape parameter p perturbing the Beta function is similar in effect to the parameter m used to the perturb the exponential distribution in generating the Weibull function, $W(\mu) = 1 - \exp(\mu^{-m})$, commonly used to fit edf data.[6])

The strength edf formed by the tensile bar data was fit using the above procedure and is shown by the aforementioned solid line. The fit was constrained by the mean flaw density determined earlier for poly3, $\lambda = 1.75\ \mu m^{-1}$ (and thus $k = 76$),[7] and the current strength bounds, resulting in best fit parameters of $\sigma_U = 5.0$ GPa, $\sigma_L = 1.9$ GPa, and $p = 1.40$, similar to those determined earlier. Once obtained, the functions $H(\sigma_f)$ and $F(\sigma_f)$ were applied in two ways. First, samples

from the same material composed of specimens of different sizes exhibit related cdf responses described by $L_1 = k_1/\lambda$ and $L_2 = k_2/\lambda$,[6-8]

$$H_2(\mu) = 1 - [1 - H_1(\mu)]^{k_2/k_1}. \quad (4)$$

Here specimen 1 was considered the tensile bar such that $k_1 = 76$. Specimen 2 was considered the bend beam, with $k_2 = 1$ or 2, and corresponding predictions of $H(\sigma_f)$ using the above parameters are shown as the right solid lines in Fig. 3. The second application obtains $f(c)$ from $F(c)$, which in turn is obtained from $1 - F(\sigma_f)$ and $\sigma(c)$. Figure 4(a) shows a plot of $f(c)$ determined in this way from $\widehat{H}(\mu)$. The flaw size population pdf is very similar to that determined earlier:[7,8] a minimum of approximately 25 nm, mode of approximately 35 nm, and skewed to larger flaw sizes with a maximum at the end of a long light tail of approximately 150 nm.

The agreement between the predicted and measured strengths of the ultra-small MEMS bend specimens in Fig. 3 suggests that the specimens are at the limit of applicability of stochastic extreme-value extrapolation, small enough to contain a single flaw and access the flaw population directly. The upper strength prediction assumes one flaw/specimen and describes much of the observed strength distribution. Such a prediction represents the population of flaws, which is directly accessed by the small stressed region within the small specimen in much the same way as notches, fillets, or particles can access a flaw population through stress localization.[7,8,14] An estimate of the size of the stressed region required to sense the flaw population without interfering extreme-value effects is given by the mean flaw spacing, $1/\lambda$, which in this case was $1/\lambda = 0.57$ μm. Figure 2(b) suggests that the extent of the active peak stresses along the fabricated beam edges was approximately 1 μm, suggesting that only one or two flaws in the central section of a beam could cause failure, consistent with the predictions of Fig. 3. Further evidence in support of this assessment is provided by Fig. 4(b), in which an SEM image of a sidewall from the RS784 fabrication run shows grain boundary grooves with spacing consistent with these values. Although not directly quantified here, the depths of the grooves inferred from tilted SEM images and AFM observations (≈50 nm)[7,35] are consistent with the flaw population estimated in Fig. 4(a).

In terms of absolute values, the beam strengths here, 2.5 GPa to 4.5 GPa, are comparable to those reported earlier for the much larger polysilicon beams noted above.[23-27] This observation suggests a commonality in both stress localization, arising from the beam geometry,[15] and flaw density, generated in polysilicon fabrication,[3,7,25,35] leading to comparable strengths. The much greater strengths, 10 GPa to 20 GPa, observed for MEMS fabricated SCS beams similar in size to

those studied here,[11,12,17,18] is then interpreted as arising from differences in the flaw population generated by different specimen preparation methods.[10] Strengths of ion beam fabricated structures are interpreted similarly.[28-34] The typically smaller strengths, 1 GPa to 4 GPa, observed for larger SCS beams,[16,19] is then mostly attributed to differences in processing and flaw population with only weak influence from extreme-value effects associated with a larger stressed area. This is the opposite effect from that observed here in comparison of tensile and bending specimens, for which processing and flaw population were identical and stochastic extreme-value effects led to weaker tensile bars relative to the bend beams.

In summary, sophisticated MEMS design and processing were used to fabricate and test ultra-small bend beams and tensile bars in a high-throughput manner. Imaging of the beams and implementation of FEA simulations enabled the maximum tensile stress in as-processed specimens to be determined, revealing microscopic and macroscopic deviations from a simple continuum beam theory estimate. A stochastic extreme-value analysis was used to predict the beam strength distribution from tests on identically-fabricated tensile bars. The stress localization inferred from the FEA, previous estimates of strength-controlling flaw density, quantitative comparison of the tensile and bending strength distributions, and SEM observations all combine to suggest that the beams were at or near the limit of size extrapolation and accessed the flaw population directly.

Data Availability Statement

The data that support the findings of this study are available from the corresponding author upon reasonable request.

Acknowledgements

B.L.B. was supported by the Center for Integrated Nanotechnologies, a Department of Energy office of Basic Energy Sciences user facility. Sandia National Laboratories is a multimission laboratory managed and operated by National Technology and Engineering Solutions of Sandia LLC, a wholly owned subsidiary of Honeywell International Inc., for the U.S. Department of Energy National Nuclear Security Administration under contract DE-NA0003525. The views expressed in the article do not necessarily represent the views of the U.S. Department of Energy, U.S. Department of Defense, or U.S. Government. Certain commercial equipment, instruments, and software are identified in this paper in order to specify the experimental procedure adequately.

Such identification is not intended to imply recommendation or endorsement by NIST or the U.S. Department of Commerce, nor is it intended to imply that the equipment or software identified are necessarily the best available for the purpose.

References

[1] M. F. Ashby, *Materials Selection in Mechanical Design*—5th Edition (Butterworth-Heinemann, New York, 2017).

[2] New market perspective for the MEMS & sensors, http://www.yole.fr/MEMS_Market.aspx#.YBbiH5eSmHs (accessed, 1/31/2021).

[3] B. L. Boyce, Exp. Mech. **50**, 993 (2010).

[4] M. S. Gaither, R. S. Gates, R. Kirkpatrick, R. F. Cook, and F. W. DelRio, J. Microelectromech. Syst. **22**, 589 (2013).

[5] S. S. Hazra, J. L. Beuth, G. A. Myers, F. W. DelRio, and M. P. de Boer, J. Micromech. Microeng. **25**, 015009 (2015).

[6] R. F. Cook and F. W. DelRio, Exp. Mechanics **59**, 279 (2019a).

[7] R. F. Cook, F. W. DelRio, and B. L. Boyce, Microsyst. Nanoeng. **5**, 49 (2019).

[8] F. W. DelRio, B. L. Boyce, J. T. Benzing, L. H. Friedman, and R. F. Cook, J. Micromech. Microeng. **30**, 125013 (2020).

[9] R. F. Cook, J. Mat. Sci. **41**, 841 (2006).

[10] F. W. DelRio, R. F. Cook, and B. L. Boyce, Appl. Phys. Rev. **2**, 021303 (2015).

[11] T. Alan, M. A. Hines, and A. T. Zehnder, Appl. Phys. Letters **89**, 091901 (2006).

[12] T. Alan, A. T. Zehnder, D. Sengupta, and M. A. Hines Appl. Phys. Letters **89**, 231905 (2006).

[13] R. F. Cook and F. W. DelRio, J. Am. Ceram. Soc. **102**, 4794 (2019b).

[14] R.F. Cook, http://doi.org/10.5281/zenodo.4024618 (accessed 1/14/2021).

[15] T. P. Weihs, S. Hong, J. C. Bravman, and W. D. Nix, J. Mater. Res. **3**, 931 (1988).

[16] C. J. Wilson, A. Ormeggi, and M. Narbutovskih, J. Appl. Phys. **79**, 2386 (1996).

[17] T. Namazu, Y. Isono, and T. Tanaka, J. Microelectromech. Syst. **9**, 450 (2000).

[18] S. Sundararajan, B. Bhushan, T. Namazu, and Y. Isono, Ultramicroscopy **91**, 111 (2002).

[19] R. Kirkpatrick, W. A. Osborn, M. S. Gaither, R. S. Gates, F. W. DelRio, and R. F. Cook, MRS Communications **3**, 113 (2013).

[20] F. W. DelRio, R. M. White, S. Krylyuk, A. V. Davydov, L. H. Friedman, and R. F. Cook, Nanotechnology **27**, 31LT02 (2016).

[21] M. Elhebeary and M. T. A. Saif, Extreme Mechanics Letters **23**, 1 (2018).

[22] M. Elhebeary, T. Harzer, G. Dehm, and M. T. A. Saif, PNAS **117**, 16864 (2020).

[23] P. T. Jones, G.C. Johnson, and R. T. Howe, Proc. SPIE **3880**, 20 (1999).

[24] L. Elbrecht and J. Binder, Sens. Mater. **11**, 163 (1999).

[25] J. N. Ding, Y. G. Meng, and S. Z. Wen, J. Mater. Res. **16**, 2223 (2001).

[26] H. Hong, J.-N. Hung, and Y.-H. Guu, Japan. J. Appl. Phys. **47**, 5256 (2008)

[27] R. Mirzazadeh, S. E. Azam, and S. Mariani, Sensors **16**, 1191 (2016).

[28] D. Di Maio and S. G. Roberts, J. Mater. Res. **20**, 299 (2005).

[29] K. Matoy, H. Schönherr, T. Detzel, T.Schöberl, R. Pippan, C. Motz, and G. Dehm, Thin Solid Films **518** 247 (2009).

[30] Y. Takahashi, H. Kondo, H. Niimi, T. Nokuo, and T. Suzuki, Sens. Actuators A **206**, 81 (2014).

[31] M. G. Mueller, M. Fornabaio, G. Zagar, and A. Mortensen, Acta Mater. **105**, 175(2016).

[32] E. D. Hintsala, S. Bhowmick, X. Yueyue, R. Ballarini, S. A. Syed Asif, W. W. Gerberich, Scripta Mater. **130**, 78 (2017).

[33] B.-S. Li, T. J. Marrow, S. G. Roberts, and D. E. J. Armstrong, JOM **71**, 3378 (2019).

[34] H. Yamaguchi, J. Tatami, T. Yahagi, H. Nakano, M. Iijima, T. Takahashi, and T. Kondo, J. Mater. Sci. **55**, 7359 (2020).

[35] E. D. Reedy, Jr., B. L. Boyce, J. W. Foulk, III, R. V. Field, Jr., M. P. de Boer, and S. S. Hazra, J. Microelectromech. Syst. **20**, 922 (2011).

[36] B. R. Lawn, *Fracture of Brittle Solids*—2nd Edition (Cambridge University Press, Cambridge, 1993).

Figures

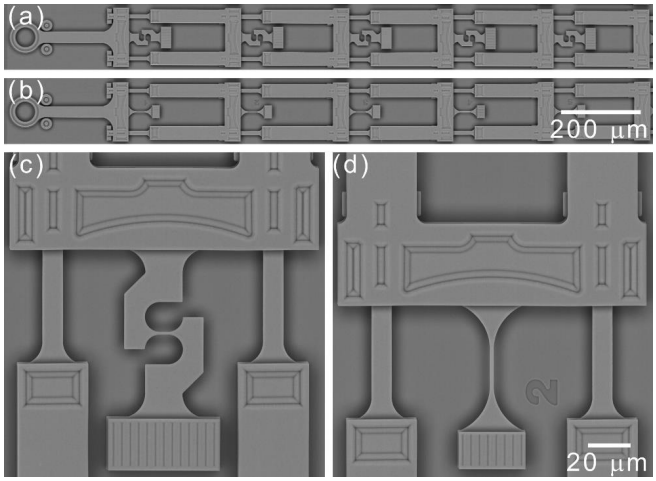

Figure 1. SEM images of the (a) bending and (b) tensile specimens. Strength testing was performed by extending the pull-tab ring at the end of each chain. Greater magnification images of the (c) bending and (d) tensile specimens. The specimens were fabricated in a single process.

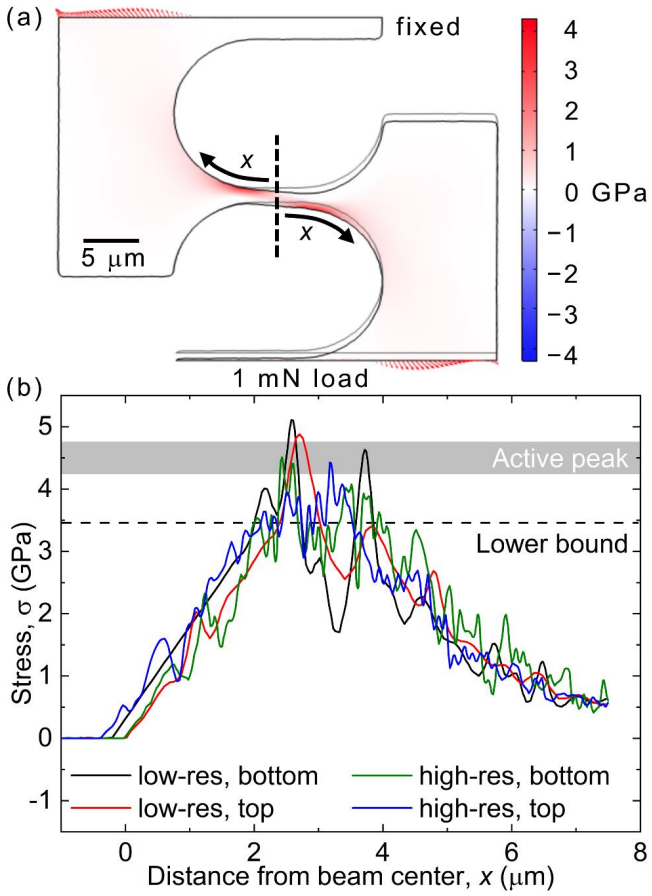

Figure 2. FEA simulations of the stresses generated in the bending specimen at two spatial resolutions. (a) Color-filled intensity map of the first principal stress in the loaded specimen from the highest resolution simulation. (b) First principal stress evaluated from both resolution simulations along the top and bottom outer fibers.

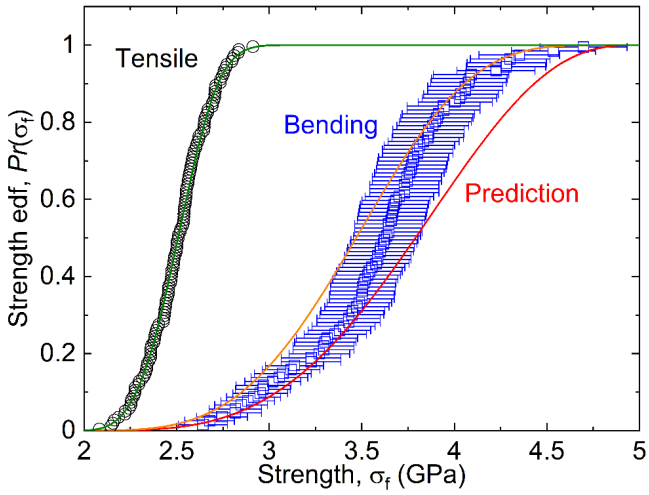

Figure 3. Strength data and empirical distribution functions for the bending and tensile specimens. The uncertainty in the strength data is ±5 % for the bending specimens and about the symbol size for the tensile specimens. The strength edfs for the bending data were predicted using the best fit parameters from the tensile data.

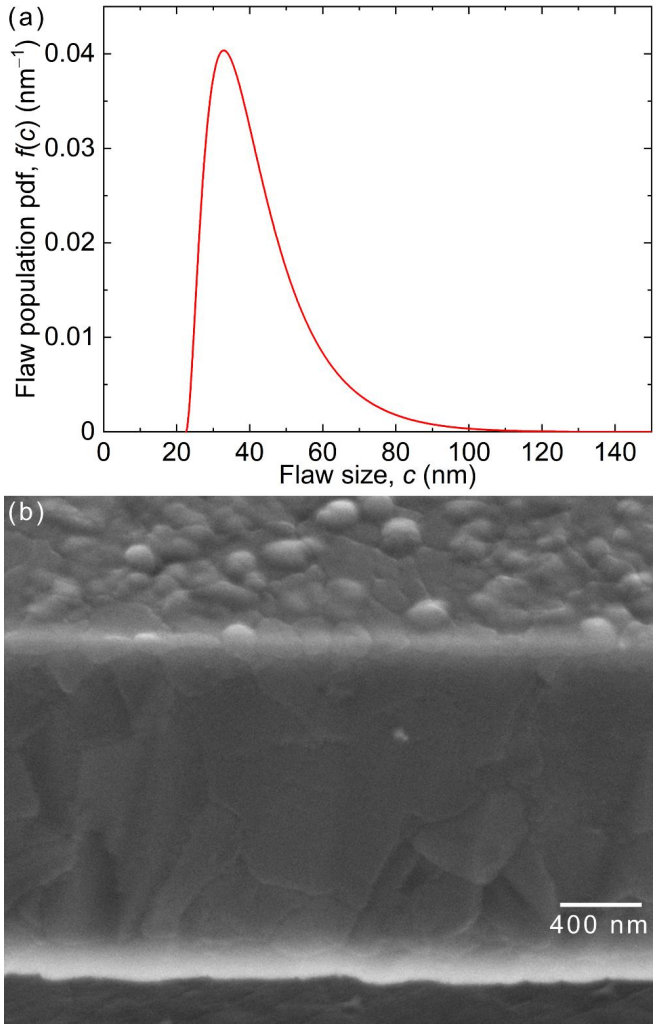

Figure 4. (a) Flaw size population pdf inferred from the tensile bar data. (b) SEM image of a sidewall surface from the fabrication process.

Applied Physics Letters ACCEPTED MANUSCRIPT

PLEASE CITE THIS ARTICLE AS DOI: 10.1063/5.0049521

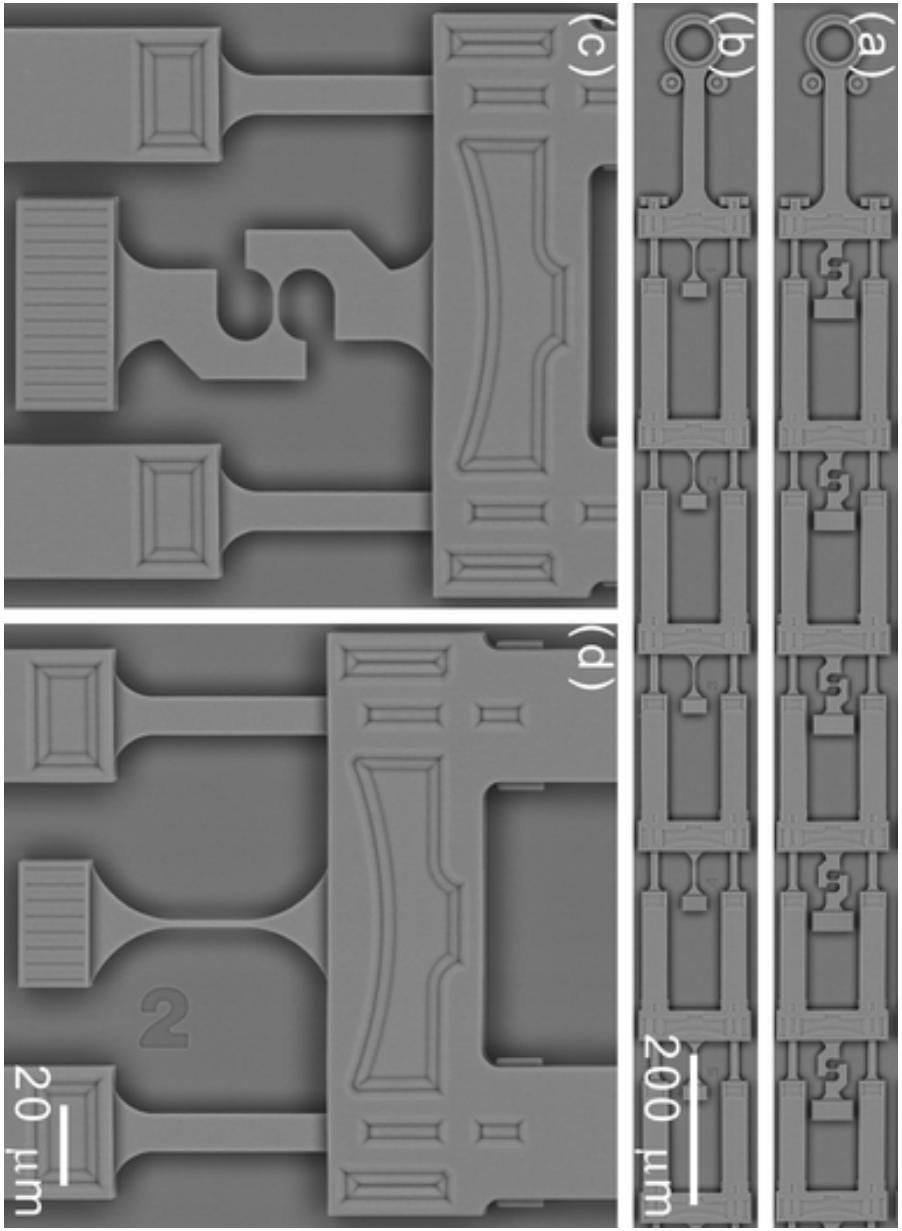

Applied Physics Letters

PLEASE CITE THIS ARTICLE AS DOI: 10.1063/5.0049521